PHYSICAL REVIEW A VOLUME 46, NUMBER 10 15 NOVEMBER 1992

Observation of surface-induced layering in bicontinuous microemulsions

Xiao-Lin Zhou
Department of Nuclear Engineering, Massachusetts Institute of Technology, Cambridge, Massachusetts 02139

Lay-Theng Lee
Laboratoire Leon Brillouin, Centre d'Etudes Nucléaires de Saclay, 91191, Gif-sur-Yvette CEDEX, France

Sow-Hsin Chen
Department of Nuclear Engineering, Massachusetts Institute of Technology, Cambridge, Massachusetts 02139

R. Strey
Max-Planck Institut für Biophysikalische Chemie, Postfach 2841, D-3400, Göttingen, Germany

(Received 8 May 1992; revised manuscript received 9 June 1992)

Neutron-specular-reflectivity measurements were made on liquid surfaces of disordered one-phase microemulsions consisting of mixtures of nonionic surfactant $C_{10}E_4$, D_2O, and octane, with equal volume fractions of water and oil, in the region of the phase diagram where the bulk microemulsion structure was known to be bicontinuous. From these measured reflectivity data, the one-dimensional scattering-length-density profiles in the vertical direction of the air-microemulsion interfaces were reconstructed directly by using a model-independent inversion scheme developed recently by one of us. From the reconstructed scattering-length-density profiles, we constructed the one-dimensional Debye correlation functions. From these correlation functions, we deduced the surface-induced layering with periods that correlate well with the bulk water-water domain average repeat distance known from a previous small-angle neutron-scattering study. We discuss in particular the effect of a finite-Q range of data on the height of the first D_2O layer.

PACS number(s): 61.12.−q, 61.25.−f, 82.70.Kj

I. INTRODUCTION

A microemulsion is a homogeneous fluid mixture, consisting of oil, water, and surfactant (amphiphilic molecules), which is thermodynamically stable and optically transparent. The transparency to light suggests that the organized microstructures in the liquid have dimensions less than the wavelength of light. Numerous small-angle scattering experiments have yielded length scales of the microstructure of the order of 100–1000 Å.

The highest mutual solubility of water and oil is observed when the hydrophilic and lipophilic tendencies of the surfactant molecules toward water and oil are approximately balanced. Detailed knowledge of the phase behavior of these systems [1] allows one to select a set of oil, water, and nonionic surfactant such as C_iE_j (n-alkyl polyglycol ether), such that a characteristic balance temperature denoted as T_{HLB} (hydrophile-lipophile balance temperature) lies in the range of temperatures from 20 to 40 °C. Figure 1 shows an example of the phase diagram of a microemulsion system consisting of n-octane-D_2O-$C_{10}E_4$. The phase diagram depicts the phase boundaries of bulk phases in the temperature-concentration (of the surfactant) plane, when the volume fractions of octane and D_2O are kept equal. Denoting by α the relative weight fraction of octane in the D_2O-octane mixture, the equal volume fraction condition leads to $\alpha=38.87\%$. In this system, the T_{HLB} is about 24 °C. At this temperature, when the surfactant concentration, denoted by γ, which is the weight fraction of $C_{10}E_4$ in the microemulsion, increases from 0% to 5%, the microemulsion shows a three-phase coexistence. Among the three bulk phases, the top layer is oil rich, the middle layer is surfactant rich, having equal volume fractions of octane and D_2O, and the lower layer is water rich. In this case, the middle layer is a microemulsion called the middle-phase microemulsion. As the surfactant concentration γ increases toward 10%, the middle phase expands until the entire sample becomes a one-phase microemulsion. Our previous small-angle x-ray and neutron-scattering experiments on a nonionic microemulsion system n-tetradecane-H_2O-$C_{12}E_5$ [2] and on an ionic microemulsion system n-decane-D_2O-AOT [3] showed conclusively that the microstructure of the one-phase microemulsions near the T_{HLB} temperature and in the range of γ from 10% to 15% is disordered bicontinuous. A disordered bicontinuous microemulsion has a microstructure which can be pictured as consisting of interpenetrating domains of oil and water, characterized by two length scales D and ξ [4]. The length D can be interpreted as the average inter-water-domain distance (or the average inter-oil-domain distance since water and oil are symmetric in the microemulsions under consideration). The length ξ is the coherent length of the local periodic domain structure. More quantitatively, D/ξ can be used as a measure of disorder due to the polydispersity of the domain sizes

[5,6].

The question arises naturally as to what is the periodic water-water domain repeating distance near the free surface of microemulsions. In 1988, Schwartz *et al.* [7] investigated x-ray reflectivity of a microemulsion surface of a three-component ionic microemulsion system consisting of decane-D_2O-AOT. This system of microemulsion, at the phase points investigated by these authors, has a microstructure consisting of a dense packing of spherical water-oil droplets [8] coated with a monolayer of sodium di-2-ethylhexylsulfosuccinate (AOT). It is clear from this small-angle neutron-scattering (SANS) experiment that the microstructure of the microemulsions was never bicontinuous. The reflectivity experiments concluded that the microemulsion surface profiles consisted of one to two layers of microemulsion droplets. The size of and the distance between droplets were consistent with the respective values of the droplets in the bulk phase. However, it has been shown by Dawson in 1987 [9] by mean-field analysis of the lattice model of microemulsions that for bicontinuous microemulsions within the middle phase, the density profiles describing the interface between oil-rich and water-rich phases are structured and nonmonotonic. Although these analyses did not address the air-microemulsion interface of one-phase bicontinuous microemulsions, it can be conjectured that the vertical density profiles of the surface in this case should also have nonmonotonic structure.

More convincing experimental evidence of surface layering on a disordered bulk liquid has come from x-ray reflectivity studies of liquid-crystal surfaces. Ocko *et al.* [10] and Pershan *et al.* [11] have studied the free surface of dodecylcyanobiphenyl (12CB) at the isotropic to smectic-*A* phase transition. At about 10 °C above T_{IA}, smectic-*A*-like ordering develops at the surface, while the bulk phase remains isotropic. More recently, Swislow *et al.* [12] studied the structure of the air–liquid-crystal interface of the lyotropic liquid crystal formed from binary mixtures of cesium perfluoro-octanoate (CsPFO) and water. As for the case of thermotropic liquid crystals, the isotropic-to-nematic phase transition has no effect on the surface structure, but as the temperature is lowered towards the nematic–smectic-*A* transition temperature, the number of surface-induced layers increases dramatically.

In this paper we analyze some experimental results which indicate that surface-induced layering also occurs in bicontinuous microemulsions. We show this by directly inverting the neutron-reflectivity data. The method of inversion of the reflectivity data can be applied to layers of any thickness on the bulk liquid-air interface. It can also be applied to films deposited on a solid substrate. This method is model independent as stated in the abstract because we do not assume beforehand any preconceived functional form for the scattering-length-density (SLD) profiles, but instead we let the inversion algorithm generate the numerical SLD value at each discrete spatial point inside the sample. We describe this method in some detail in this paper, together with the analysis of a series of neutron-reflectivity data measured on bicontinuous one-phase microemulsions.

II. REFLECTIVITY MEASUREMENTS

The vertical scattering-length-density profiles of bulk liquid surfaces of disordered one-phase microemulsions consisting of a nonionic surfactant $C_{10}E_4$, D_2O, and octane were studied by neutron-reflectivity measurements at three phase points, as indicated by the solid dots in the phase diagram shown in Fig. 1. The microemulsion samples were prepared using D_2O of 99.75% isotopic purity, *n*-octane of 99.50% purity, and $C_{10}E_4$ which was purified using the three-phase extraction technique (3PHEX) [13]. The compositions of the samples were specified by weight, and they contained equal volume fractions of water and octane. This latter constraint corresponds to specifying

$$\alpha=\frac{\mathrm{oil(wt)}}{\mathrm{oil(wt)+water(wt)}}\ .$$

The amount of surfactant $C_{10}E_4$ is specified by its weight fraction γ defined as

$$\gamma=\frac{\mathrm{surfactant(wt)}}{\mathrm{oil(wt)+water(wt)+surfactant(wt)}}\ .$$

For reflectivity measurements, the sample was placed in a container of ($9.5\times29\times2$ mm^3) made of aluminum and equipped with a thermocouple to control the sample temperature to a precision of 0.01 °C. The container was enclosed in an inner cell with quartz windows, which in turn was enclosed by an outer cell also with quartz windows, the latter of which served to help maintain constant the temperature of the air between the two cells.

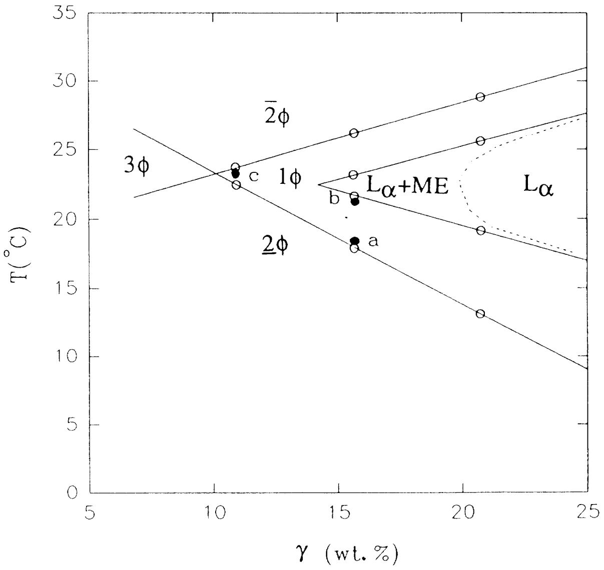

FIG. 1. The phase diagram of a microemulsion system consisting of *n*-octane/D_2O/$C_{10}E_4$. The horizontal axis is the weight fraction γ of $C_{10}E_4$ and the vertical axis is the temperature T in degrees Celsius. The straight lines denote the boundaries between any two phases. The solid dots indicate the positions in the phase diagram of the three microemulsions measured in this study. The circles with a dot inside each indicate the experimental points used to construct the phase diagram.

This arrangement minimized the evaporation and condensation of the alkane and water on the cell windows during the data acquisition period, which was about 6 h per measurement.

The neutron-reflectivity measurements were taken on the time-of-flight reflectometer DESIR at the ORPHEE reactor at Saclay, France. The incident angle was 0.71° and the neutron wavelengths ranged from 3 to 15 Å. with high-purity solvents, the angular resolution was determined to be 5%. Concerning the samples, in all cases, the initial equal volume fractions of water and oil in the microemulsion samples were modified somewhat due to evaporation of the solvents in spite of the precautions taken. The first and second measurements were made on samples with $\gamma = 15.77\%$ at temperatures 18.50 and 21.00 °C, respectively. The third measurement was for $\gamma = 10.55\%$ at temperature 23.20 °C. These conditions correspond to the three solid dots in the phase diagram in Fig. 1. The evaporation at the air-microemulsion surface had the effect of increasing the effective surfactant concentration γ. From Fig. 1 it is seen that a moderate amount of evaporation will leave the three-phase points remaining in the one phase state. The evaporation-modified parameters of the microemulsion samples in the three experiments are listed in Table I in comparison with the pre-evaporation values.

The first measurement, corresponding to the sample initially at $\gamma = 15.77$ at $T = 18.50\,^\circ\mathrm{C}$, is at the phase point close to the 1-2 phase boundary. The reflectivity data were obtained in the Q range of 0.011–0.44 (1/Å), where $Q = 4\pi \sin\theta/\lambda$ is the neutron wave-vector transfer. The data are plotted in circles as a function of Q in Fig. 2(a). In this figure, a peculiar feature in the Q dependence of the reflectivity is the flatness of the curve in the region $Q = 0.02$–0.04 (1/Å) and a gentle peak at around $Q = 0.031$ (1/Å). For other experiments we have analyzed, the reflectivity usually decreases smoothly. This difference implies some special feature in the real-space scattering-length-density profile of the microemulsion surfaces. Since, according to the simulated result of a previous paper [12], an oscillatory variation in the scattering-length-density profile can produce this kind of flatness and reflectivity peak in a region of Q after the critical edge, we expect that these features in the tail portion of the measured reflectivity indicate the existence of oscillations in the scattering-length-density profile of the microemulsion surface. To verify this, the real-space scattering-length-density profile is reconstructed by the direct inversion of the data in Sec. III.

In the second measurement, the sample is at $\gamma = 15.77$ and $T = 21.00\,^\circ\mathrm{C}$ at the beginning. This point is close to the $L\alpha$ phase boundary. The data are plotted in circles as a function of Q in Fig. 3(a). In this figure, features similar to those in the previous experiment were observed. The difference between this plot and the previous one is that the peak in Fig. 3(a) is more pronounced and that the valley before the peak is better defined. The peak position occurs at $Q = 0.034$ (1/Å), as compared to 0.031 (1/Å) above. This might mean that the oscillations in the real-space scattering-length-density profile are more pronounced and the period of oscillations slightly smaller than that of the previous experiment.

TABLE I. Initial values of the composition parameters of the microemulsions compared with their effective values after the evaporation effect is considered.

T (°C)	α (%) (initial)	α' (%) (effective)	γ (%) (initial)	γ' (%) (effective)
18.50	38.87	30.60	15.77	17.40
21.00	38.87	32.19	15.77	17.07
23.20	38.87	32.23	10.55	11.46

In the third measurement, the sample is initially at $\gamma = 10.55$ and $T = 23.20\,^\circ\mathrm{C}$. From Fig. 1, this point is close to the three-phase coexistence boundary. The data are plotted in circles as a function of Q in Fig. 4(a). In

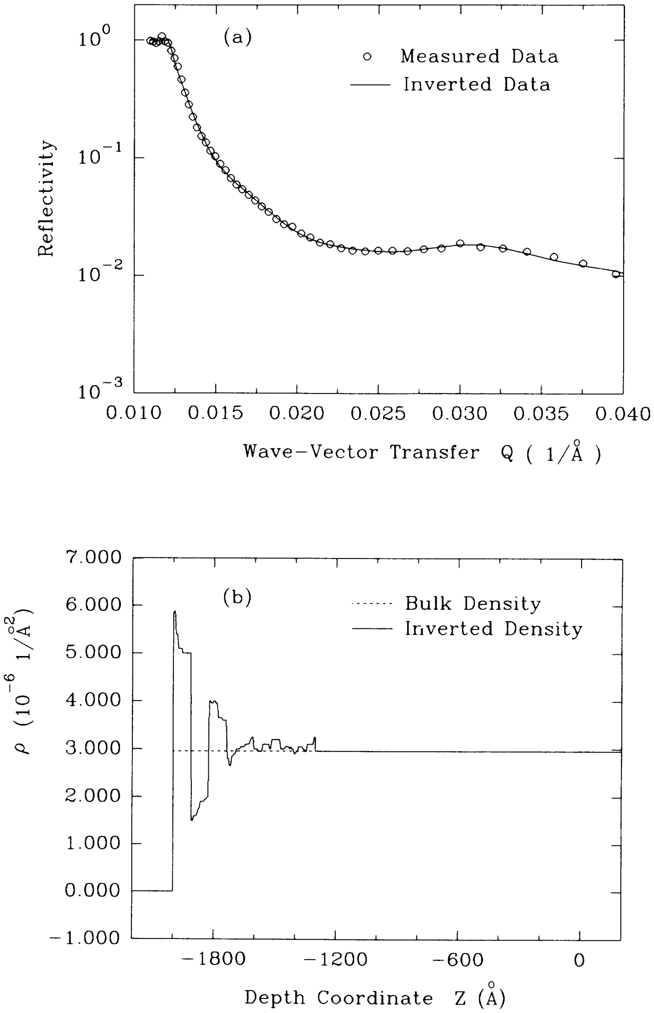

FIG. 2. The reflectivity data and their inversion for the microemulsion at $\gamma = 15.77\%$ (effective value: $\gamma = 17.40\%$) and $T = 18.50\,^\circ\mathrm{C}$: (a) The measured neutron reflectivity (circles) and the reflectivity (solid line) calculated from the inverted profile in (b), as a function of wave-vector transfer Q. (b) The inverted scattering-length-density profile from the data (circles) in (a). The dashed line indicates the bulk density level of the microemulsion which is 2.96×10^{-6} (1/Å^2).

this figure, there is a bump at $Q=0.02$ (1/Å). The position of the bump $Q=0.02$ Å^{-1} in Fig. 4(a) is quite different form those of the peaks in the previous two experiments [Figs. 2(a) and 3(a)]. The physical meaning of this difference is difficult to assess, and it will be made clear by inverting the data directly to produce the SLD profile.

In all three experiments, the error bars of the data are a function of Q and increase as Q increases. However, since the SLD profiles of the samples are to be constructed using the data at all experimental Q points, the error bars in the inverted SLD profiles will depend on the maximum error of the data. The maximum error in these three sets of data is estimated to be 6%, and this error will be used to evaluate the errors in the inverted SLD profiles in Sec. III.

The measured reflectivity data are not corrected for the roughness effect of the air-microemulsion interface because it is negligible for the Q range (<0.04 Å^{-1}) in Figs. 2(a), 3(a), and 4(a). This can be proven as follows: The Debye-Waller factor for a typical roughness of 10 Å at a typical point $Q=0.02$ Å^{-1} is

$$\mathrm{DW}=e^{-2k_0k_b\sigma^2}\approx e^{-(Q\sigma)^2/2}\approx e^{-0.02}\approx 0.98\ . \qquad (1)$$

where k_b is the wave number in the bulk microemulsion. Obviously, the difference is only 2%, less than the 6% experimental error discussed in the previous paragraph. This also guarantees that any appreciable features observed in the SLD profiles are not artifacts due to the uncorrected surface-roughness effect.

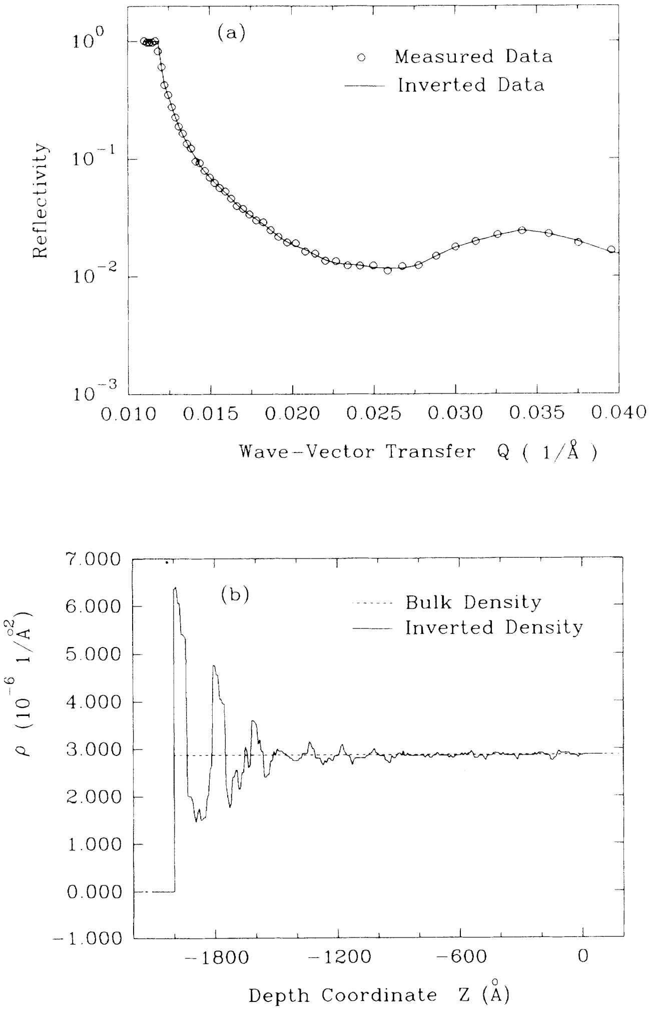

FIG. 3. The reflectivity data and their inversion for the microemulsion at $\gamma=15.77\%$ (effective value: $\gamma=17.07\%$) and $T=21.00$ °C: (a) The measured neutron reflectivity (circles) and the reflectivity (solid line) calculated from the inverted profile in (b), as a function of wave-vector transfer Q. (b) The inverted scattering-length-density profile from the data (circles) in (a). The dashed line indicates the bulk density level of the microemulsion which is 2.87×10^{-6} (1/Å^2).

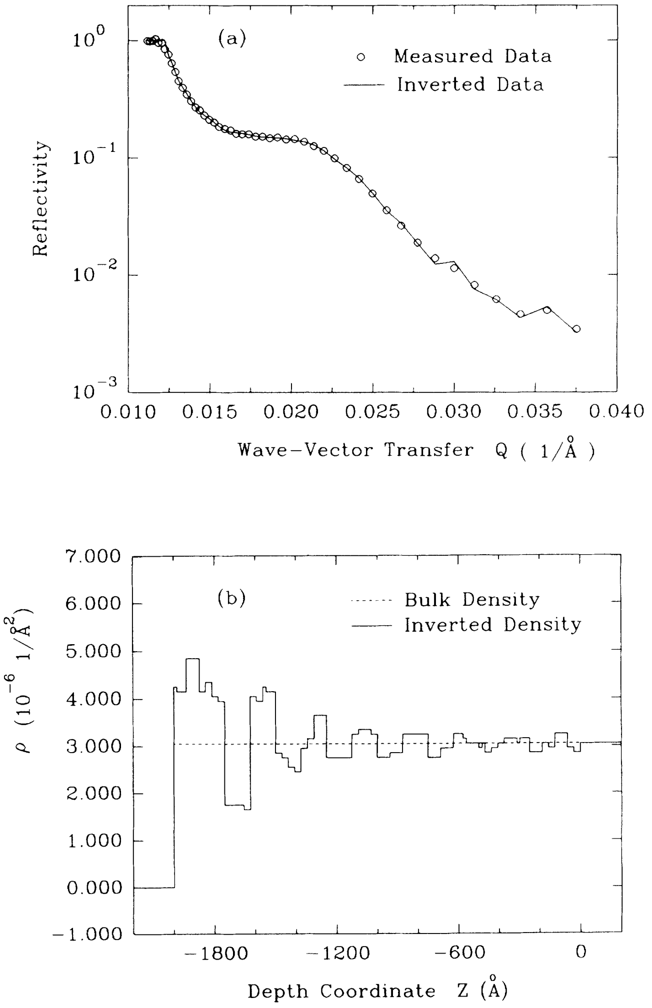

FIG. 4. The reflectivity data and their inversion for the microemulsion at $\gamma=10.55\%$ (effective value: $\gamma=11.46\%$) and $T=23.20$ °C. (a) The measured neutron reflectivity (circles) and the reflectivity (solid line) calculated from the inverted profile in (b), as a function of wave-vector transfer Q. (b) The inverted scattering-length-density profile from the data (circles) in (a). The dashed line indicates the bulk density level of the microemulsion which is 3.05×10^{-6} (1/Å^2).

III. INVERSION OF REFLECTIVITY DATA

A. Methodology

The scattering-length-density profile of a microemulsion surface may be described as a superposition of some functional variation on top of a constant bulk density ρ_b. Therefore, a convenient coordinate system can be set up such that the infinite region $(0,\infty)$ to the right of the origin corresponds to the bulk microemulsion characterized by a constant scattering-length density ρ_b, the finite region $(-d,0)$ to the left of the origin contains the deviation $\rho(z)-\rho_b$ of the scattering-length density from the bulk, and the region $(-\infty,-d)$ is air. When a plane neutron wave $e^{ik_0 z}$ impinges from the air onto the surface at $z=-d$ and undergoes a specular reflection, it is known that the waves in the three regions satisfy the one-dimensional Helmholtz wave equation [14]. Using the Green's-function method, the reflectance r can be formally expressed as [15]

$$r=Re^{-2ik_0 d}-\frac{4\pi i}{k_0+k_b}e^{i(k_b-k_0)d} \times \int_{-d}^{0} dz'(\rho(z')-\rho_b)U(z')e^{ik_b z'} . \qquad (2)$$

Here $R=(k_0-k_b)/(k_0+k_b)$, k_0 and $k_b=(k_0^2-4\pi\rho_b)^{1/2}$ being the wave number in the air and in the bulk, respectively. $U(z)$ is the one-dimensional wave function of a neutron in the film. Equation (2) states that the reflectance r is equal to a superposition of the contribution due to the effect of the variation of $\rho-\rho_b$ on top of the known bulk Fresnel reflection R. When the contribution by $\rho-\rho_b$ is small, the position of the critical edge is mainly determined by the bulk density ρ_b, and conversely, one can determine the bulk density of the microemulsion from the measured location of the critical edge. This is a good approximation when there is little variation of the density profile or when the variation comes in an oscillatory form such that $\rho-\rho_b$ changes sign as z increases and thus the integral in Eq. (2) is small although $\rho-\rho_b$ might be large at some values of z. This is also true when the density deviation from the bulk is confined to a very narrow region (i.e., small d). By this token, the bulk scattering-length-density values were determined from the positions of the critical edge shown in Figs. 2(a), 3(a), and 4(a). They are 2.96×10^{-6}, 2.87×10^{-6}, and 3.05×10^{-6} ($1/\text{Å}^2$) for the three measurements, respectively. Since the corresponding values without octane evaporation should be 2.51×10^{-6}, 2.51×10^{-6}, and 2.65×10^{-6} ($1/\text{Å}^2$), respectively, the effective γ' values are 17.40%, 17.07%, and 11.46%, and the effective α' values are 30.60%, 32.19%, and 32.23%, respectively (Table I). Note that these values are estimated from the reflectivity data averaged over 6 h.

Once the bulk densities are determined, they are used as the initial conditions for the inversion of the reflectivity data to reconstruct the functional form of the density variations. When the density profile is given, the most efficient method for the calculation of reflectivity is the use of a recursion relation [16] given by Parratt. This recursion relation also follows trivially from the solution of the one-dimensional Schrödinger equation in a homogeneous layer bounded by interfaces i and $i+1$. In this method, the density profile is digitized into N discrete layers, where N can be very large for a good approximation. The relation is

$$r_i=\frac{R_{i+1}+r_{i+1}e^{2ik_{i+1}\Delta z_{i+1}}}{1+R_{i+1}r_{i+1}e^{2ik_{i+1}\Delta z_{i+1}}} . \qquad (3)$$

Here the index i indicates that the quantity pertains to the ith layer. The layers are numbered $1,2,\ldots,N$ with layer N bordering on the constant bulk and layer 1 facing the air. R_{i+1} represents the Fresnel reflection coefficient of the interface between layer i and layer $i+1$. k_{i+1} and Δz_{i+1} are the wave number and the thickness of layer $i+1$, respectively. r_i is defined as the reflection coefficient from a system composed of the substrate plus layers $i+1$ to N when an incident plane wave propagates in a half-space medium with wave number k_i and impinges on layer $i+1$. $r_N=0$ because the profile smoothly merges into the bulk. From k_N and k_{N-1} of the first two layers next to the bulk, one can calculate

$$R_N=(k_{N-1}-k_N)/(k_{N-1}+k_N) .$$

Substituting r_N, R_N, k_N, and Δz_N into Eq. (3), one obtains r_{N-1}. Using r_{N-1},

$$R_{N-1}=(k_{N-2}-k_{N-1})/(k_{N-2}+k_{N-1}) ,$$

k_{N-1}, and Δz_{N-1}, one obtains r_{N-2}. This recursion goes on until r_0, which is obviously the reflection coefficient from the entire system, and $|r_0|^2$ is what is measured experimentally.

Obviously, r_0 is an analytical function of N variables ρ_i ($i=1,2,\ldots,N$), though the functional form is complex and highly nonlinear for large N. For convenience, the index "0" is dropped from the N-layer reflection coefficient r_0, and one can write formally

$$r(k_0)=P(k_0,\bar{\rho}) , \qquad (4)$$

where P is an analytical function to be calculated by the recursion relation and $\bar{\rho}=\{\rho_1,\rho_2,\ldots,\rho_N\}$ is an N-dimensional vector representing the scattering-length-density values at N positions. Taking the squared modulus of Eq. (4) and equating it to the M reflectivity data at k_0^i ($i=1,2,\ldots,M$), one has a set of M simultaneous equations, which can be written as

$$\varepsilon_i=\big||r(k_0^i)|^2-|P(k_0^i,\bar{\rho})|^2\big|=0 \qquad \text{for } i=1,2,\ldots,M , \qquad (5)$$

where $M=52$, 51, and 48 for our three experiments, respectively. Because experimental data contain errors, there exists no solution ρ_i ($i=1,2,\ldots,N$) which satisfies Eq. (5) simultaneously in the exact sense. Equation (5) can only be satisfied by a set of ρ_i ($i=1,2,..,N$) within an error bound commensurate with the experimental errors. This means one should consider a vector $\bar{\rho}$ as a solution to Eq. (5) as long as it makes ε_i smaller than the error bar of the data $|r(k_0^i)|^2$ for all the data points.

Quantitatively, this is equivalent to solving the following equation:

$$E_i = \left| \frac{|r(k_0^i)|^2 - |P(k_0^i,\bar{\rho})|^2}{\sigma_i} \right| \le 1 \quad \text{for } i=1,2,\ldots,M \; . \qquad (6)$$

To solve this set of equations, we have devised a method called the groove tracking method (GTM) [17] which enables us to approach the solution in a computationally efficient way. It is based on the understanding that there exists a groove in the N-dimensional vector space leading to the solution monotonically. As long as we reach the groove at the beginning and then, as we proceed, bind ourselves to the groove like a roller coaster binds itself to the track, we can avoid the necessity of mapping the whole space, which is time inefficient and infeasible for the case of neutron reflection (10^N possibilities for N layers even if each layer is allowed to vary for as few as ten times). The numerical implementation of this technique is described in a separate paper [17].

B. Testing of method using simulated data: Effect of the finite-Q range

The reliability of this method as applied to the inversion of microemulsion reflectivity data is first investigated through testing on simulated reflectivity data. The input profile used is shown by the dashed line in Fig. 5(b), and the corresponding reflectivity is calculated and plotted in circles in Fig. 5(a). A Gaussian noise is then introduced into the data to simulate experimental errors. The Q range of the simulated data is 0.002–0.1 Å^{-1}. The simulated reflectivity data are then fed into the inversion program described above, and the bulk density of the profile is manually entered as the initial condition. The inversion program is started and, when it stops, a real-space profile is reconstructed and plotted as a solid line in Fig. 5(b). This profile is a very close digitized replication of the original profile indicated by the dashed line. The reflectivity calculated from the digitized reconstruction is plotted as a solid line in Fig. 5(a), and close agreement is obtained with the original simulated data. The small difference between the original and the reconstructed profiles comes from the Gaussian noise introduced into the exact simulated data. This shows the reliability of the inversion method for this kind of profile.

The effect of the finite-Q range of the experimental data on the features of the inverted profile is also investigated. We did this by truncating the data in Fig. 5(a) at $Q=0.06$ and 0.03 (1/Å), as indicated in Figs. 6(a) and 7(a). Inversion was carried out for both cases, and the reconstructed profiles were plotted in solid lines in Figs. 6(b) and 7(b). The reflectivities calculated from these reconstructed profiles are plotted in solid lines in 6(a) and 7(a), respectively. It is observed in Fig. 6(b) that the truncation of the data at $Q=0.06$ (1/Å) has the effect of artificially lowering the peak value of the first high-density layer on the surface of the profile. The effect is more severe when the truncation occurs at $Q=0.03$ (1/Å). The second effect is periodicity of the profile. It is seen, from Fig. 6(b), that truncation at $Q=0.06$ has preserved the correct periodicity of the original profile, while from Fig. 7(b), the periodicity is not well preserved. The reason for this is that the first truncated data set has retained the peak at $Q=0.035$ (1/Å), while the second has not. This means that, in order to preserve the surface height as well as the periodicity of the actual profile, the experimental Q range should be large enough. Knowing the effect of finite-Q range on the degradation of the reconstructed profile, we will be able to understand better the reconstructed profiles from the real data in Sec. III C.

C. Inversion of Experimental Data

By means of the method discussed above, the three sets of data as shown by circles in Figs. 2(a), 3(a), and 4(a)

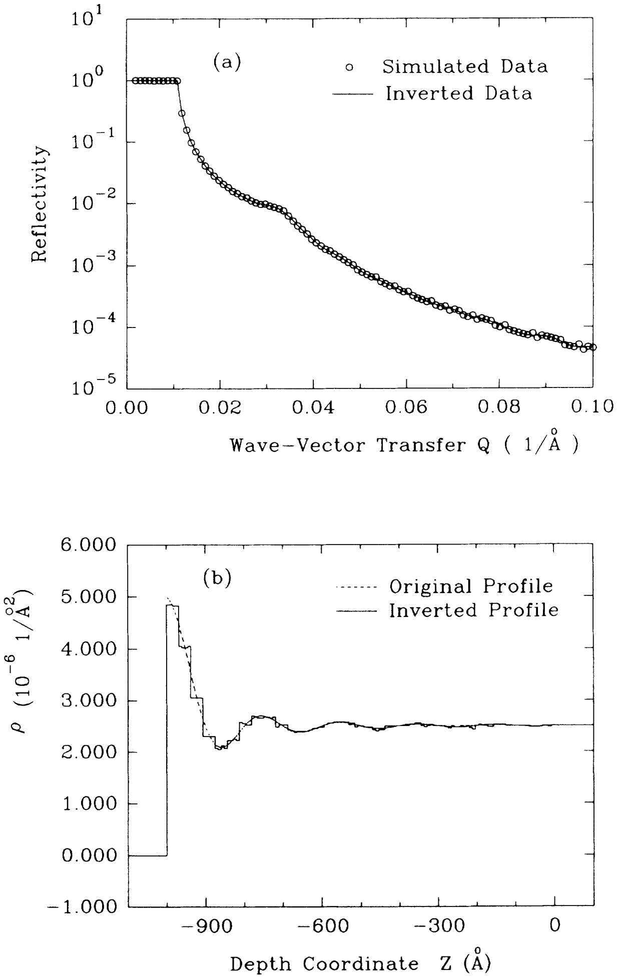

FIG. 5. The simulated reflectivity data and their inversion for the initial profile shown by the dashed line in (b) (a) The simulated neutron reflectivity (circles) and the reflectivity (solid line) calculated from the inverted profile in (b), as a function of wave-vector transfer Q. The Q range is 0.002–0.1 (1/Å). A Gaussian noise is introduced into the data to imitate real experimental errors. (b) The inverted scattering-length-density profile from the data (circles) in (a). The dashed line indicates the original profile.

were inverted to obtain the corresponding real-space scattering-length-density profiles plotted in solid lines in Figs. 2(b), 3(b), and 4(b). The dashed lines are the average bulk density levels of the microemulsions. The reflectivities calculated from these reconstructed profiles are plotted in sold lines in Figs. 2(a), 3(a), and 4(a), respectively. The agreement between the measured data (circles) and the calculated reflectivities (solid lines) based on the inverted profiles was excellent (the χ^2 variance of the fit is about unity). Note that the same ranges of ordinates are used in Figs. 2(a), 3(a), and 4(a) for the sake of visualizing the differences among the reflectivity curves.

The errors of the inverted SLD profiles in Figs. 2(b), 3(b), and 4(b) can be evaluated as follows. Since the maximum error of the measured reflectivity occurs at the higher end of the data Q range, a large-Q approximation can be used to express the maximum error in SLD profiles in terms of the maximum error in the reflectivity data. The reflectivity $|r|^2$ at large Q can be written as

$$|r|^2 \sim \frac{\rho^2}{Q^4} . \tag{7}$$

Therefore, one has

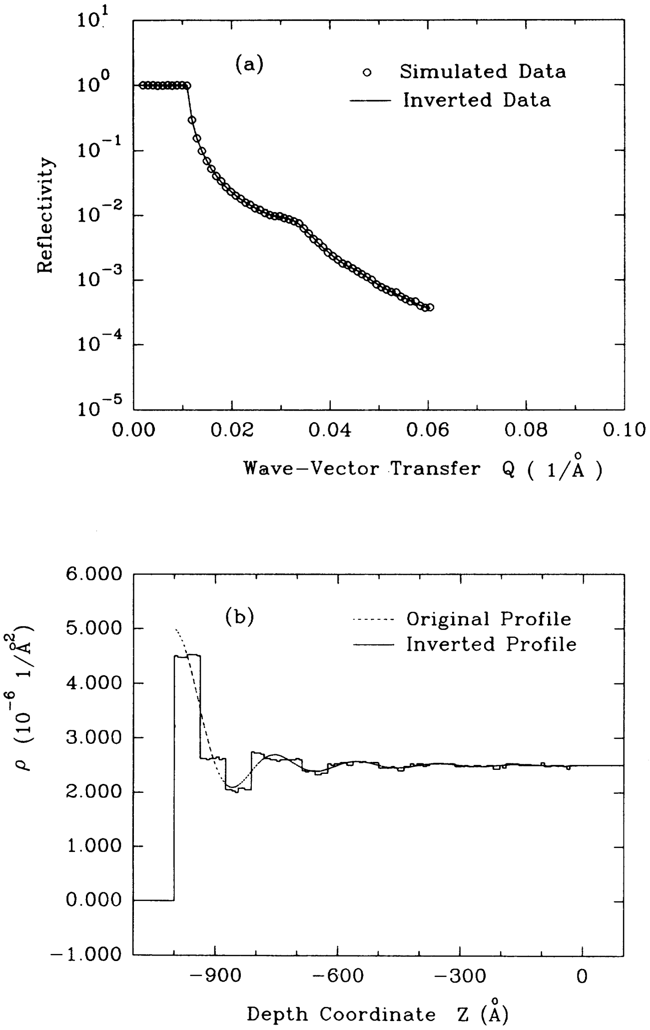

FIG. 6. The simulated reflectivity data and their inversion for the initial profile shown by the dashed line in (b). The original profile used to generate the simulated data is the same as that in Fig. 5. However, the data range is truncated to 0.002–0.06 (1/Å) into investigate the effect of truncation on the degradation of the inverted profile as compared to that in Fig. 5. (a) The simulated neutron reflectivity (circles) and the reflectivity (solid line) calculated from the inverted profile in (b), as a function of wave-vector transfer Q. A Gaussian noise is introduced into the data to imitate real experimental errors. (b) The inverted scattering-length-density profile from the data (circles) in (a). The dashed line indicates the original profile.

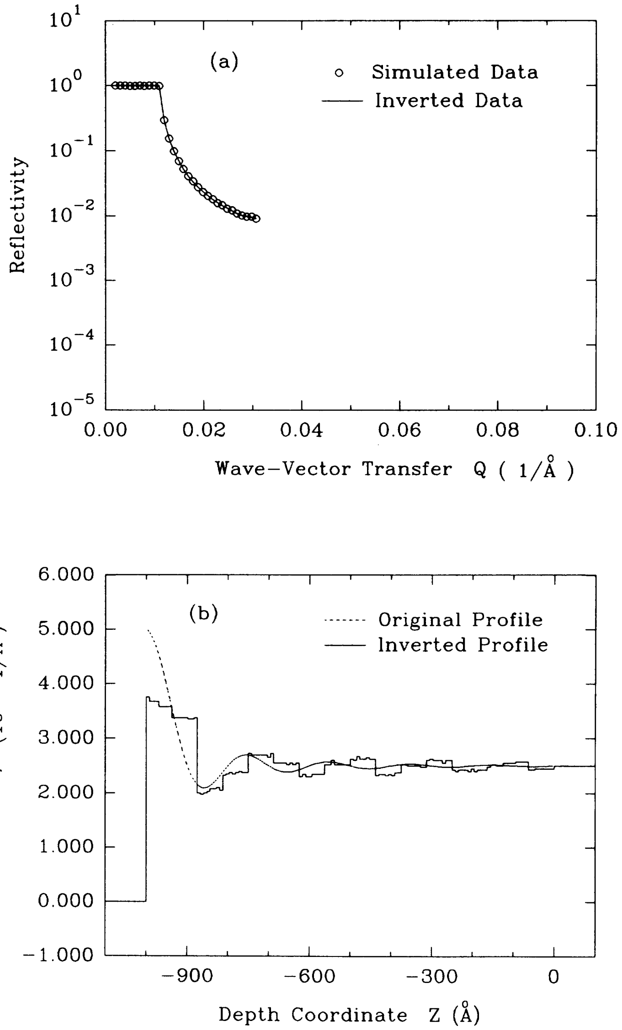

FIG. 7. The simulated reflectivity data and their inversion for the initial profile shown by the dashed line in (b). The original profile used to generate the simulated data is the same as that in Fig. 5. However, the data range is truncated to 0.002–0.03 (1/Å) to investigate the effect of truncation on the degradation of the inverted profile as compared to that in Figs. 5 and 6. (a) The simulated neutron reflectivity (circles) and the reflectivity (solid line) calculated from the inverted profile in (b), as a function of wave-vector transfer Q. A Gaussian noise is introduced into the data to imitate real experimental errors. (b) The inverted scattering-length-density profile from the data (circles) in (a). The dashed lines indicates the original profile.

$$\frac{\delta\rho}{\rho}=\frac{1}{2}\frac{\delta|r|^2}{|r|^2} . \tag{8}$$

This means that the relative error in ρ is half that in $|r|^2$. Denoting the error bar in ρ as σ_z and that in the $|r|^2$ as σ_Q, one has

$$\frac{\sigma_z}{|\rho|}=\frac{1}{2}\frac{\sigma_Q}{|r|^2} . \tag{9}$$

Using Eq. (9), it is estimated that the relative error of the SLD profiles in Figs. 2(b), 3(b), and 4(b) is $\sigma_z/|\rho|=3\%$ using the maximum relative error $\sigma_Q/|r|^2=6\%$ as discussed at the end of Sec. II. The effect of the error bars should be kept in mind when one tries to interpret the data and the inverted profiles, although the error bars at individual data points in Figs. 2, 3, and 4 are left out for ease of visualization.

It should be pointed out that the reflectivities represented by the solid lines in Figs. 2(a), 3(a), and 4(a) were calculated at exactly the experimental Q values. The solid lines are obtained by connecting the discrete calculated points by straight-line segments. Under this consideration, one should refrain from interpreting the discontinuous appearance of the tail section of the solid line in Fig. 4(a) as an indication of a discontinuous nature of the reflectivity curve versus Q. In fact, if the reflectivity is calculated at more closely spaced Q points and connected by shorter straight-line segments, the reflectivity curve will look smooth in the tail section of Fig. 4(a). This also suggests that the experimental Q intervals are too large in this region of Q to resolve the smooth variation of the reflectivities.

In reconstructing the profiles in Figs. 2(b), 3(b), and 4(b), we used the bulk densities as the initial conditions. However, we have shown that the final inverted SLD profile does not depend on the choice of the initial condition through testing the model-independent inversion method on the reflectivity data under various initial conditions. The reason for choosing the bulk densities as the initial conditions is to save computation time. In addition, for all three microemulsion samples, the thickness of the structured surface region is chosen to be 2000 Å, which is conservative in consideration of the detectable depth of the neutron.

Finally, we would like to stress that the inverted profiles in Figs. 2(b), 3(b), and 4(b) are obtained without any preassumed models, i.e., model independently. The SLD value at each discretized spatial point in the surface region was generated self-consistently by the inversion algorithm. In fact, before the data were inverted, we did not know what kind of shape the SLD profiles would take. It is the direct model-independent inversion that produced objectively the oscillating shapes in Figs. 2(b), 3(b), and 4(b). This distinguishes the present inversion method from the conventional model fitting.

D. Surface Debye correlation functions

One common feature in Figs. 2(b), 3(b), and 4(b) is that the scattering-length density is highest in the surface layer of the microemulsion, and the density profiles oscillate with damping and gradually merge into the bulk values. However, the height of the surface layer differs among the three cases. We will discuss the reason for this difference. Another feature of the inverted profiles is the periodicity of the density fluctuations, i.e., the layered structure. The period and other properties will be discussed in Sec. IV.

To better understand the density profiles, the reconstructed profiles in Figs. 2(b), 3(b), and 4(b) are used to compute the following Debye correlation functions of the

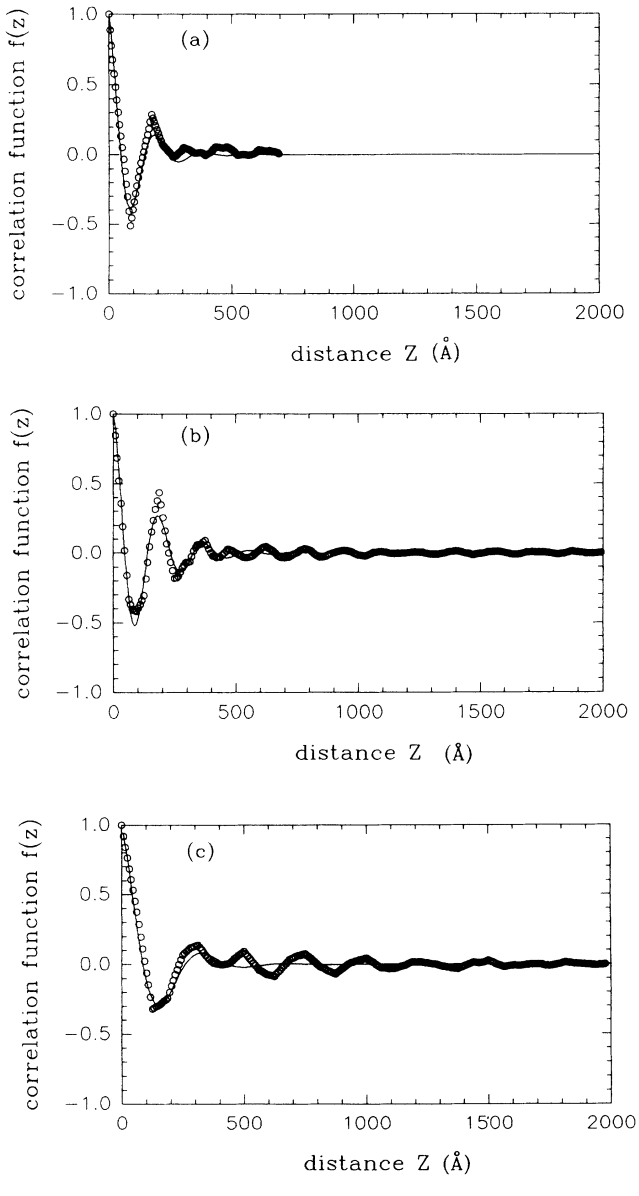

FIG. 8. The Debye correlation functions calculated from Eq. (10) (circles) and Eq. (12) (solid line) of the surface density structures: (a) $\gamma=15.77\%$ (effective: $\gamma'=17.40\%$) and $T=18.50\,^\circ\mathrm{C}$. The fitted parameters for Eq. (12) are $\xi=96$ Å and $D=196$ Å. (b) $\gamma=15.77\%$ (effective: $\gamma'=17.07\%$) and $T=21.00\,^\circ\mathrm{C}$. The fitted parameters for Eq. (12) are $\xi=140$ Å and $D=187$ Å. (c) $\gamma=10.55\%$ (effective: $\gamma'=11.46\%$) and $T=23.20\,^\circ\mathrm{C}$. The fitted parameters for Eq. (12) are $\xi=132$ Å and $D=348$ Å.

surface structures of the microemulsions:

$$f(z)=\frac{\int_{-d}^{0}\Delta\rho(z')\Delta\rho(z+z')dz'}{\int_{-d}^{0}\Delta\rho^2(z')dz'}\ , \tag{10}$$

$\Delta\rho(z)=\rho(z)-\rho_b$ denotes the fluctuation around the bulk density. This dimensionless function essentially represents the degree of ordering in one dimension perpendicular to the surfaces of microemulsions. The physical meaning of the surface Debye correlation function defined by Eq. (10) is that $f(z)$ signifies how the SLD density fluctuates with regard to the SLD value at the air-microemulsion interface. In other words it is a conditional probability of finding a certain SLD density level at a distance z from the surface position, given the existence of the air-microemulsion interface.

The correlation functions as defined by Eq. (10) are calculated directly suing the SLD profiles in Figs. 2(b), 3(b), and 4(b) and plotted in circles in Figs. 8(a), 8(b), and 8(c), respectively. Since it was known from scattering experiments that the Debye correlation function in a three-dimensional bulk microemulsion takes the following form:

$$f(r)=\frac{\sin(kr)}{kr}e^{-r/\xi}\ ,\quad k\equiv\frac{2\pi}{D} \tag{11}$$

it is natural to generalize that the correlation function $f(z)$ in a one-dimensional microemulsion should take the one-dimensional version of Eq. (11). Therefore, the dominant part of each of the calculated correlation functions should be capable of being approximately fitted to the following analytic form:

$$f(z)=e^{-z/\xi}\cos\left[\frac{2\pi z}{D}\right]\ . \tag{12}$$

As expected, the dominant part of the circles in Figs. 8(a)-8(c) can be fitted fairly closely into the form of Eq. (12). The fitted curves are plotted in solid lines in Figs. 8(a)–8(c). In Eq. (12), ξ denotes the decay length of the oscillation and D the period of the oscillation induced by the surface perturbation. In Fig. 8(a), the fitted parameters are (see Table II) $\xi=96$ Å and $D=196$ Å. In Fig. 8(b), $\xi=140$ Å and $D=187$ Å. In Fig. 8(c), $\xi=132$ Å and $D=348$ Å. The reason that the correlation functions roughly take the form of Eq. (12) up to the second peak is that a surface perturbation propagating into the bulk assumes a damped sinusoidal form due to the bicontinuous nature of the microemulsions under the condition of equal water and oil volume fractions. In Figs. 8(b) and 8(c), oscillation are seen after the second peak. We do not discuss them because they are less important compared with the second peak which represents the nearest-neighbor correlation. However, they can be fitted into another term of the form of Eq. (12) but with different parameters ξ and D. In that case, the difficulty would be how to associate proper physical meaning with the extra parameters.

IV. DISCUSSION OF RESULTS

The scattering-length densities of the three constituents of the microemulsions studied in this paper are estimated to be 6.398×10^{-6}, 0.112×10^{-6}, and -0.522×10^{-6} $(1/\text{Å}^2)$ for D_2O, $C_{10}E_4$, and octane, respectively. Therefore, a density higher than 0.112×10^{-6} $(1/\text{Å}^2)$ must contain D_2O and a density lower than 6.398×10^{-6} $(1/\text{Å}^2)$ must contain octane or $C_{10}E_4$. For a given surfactant content, there is a one-to-one correspondence between the scattering-length density and the D_2O or octane volume fraction. Due to this simple relation, it is possible to interpret the reconstructed scattering-length-density profiles shown in Figs. 2(b), 3(b), and 4(b) directly in terms of the D_2O density distribution in the air-microemulsion interfaces. The Debye correlation functions shown in Figs. 8(a)–8(c) can be similarly understood in terms of the D_2O correlations. Although some evaporation of octane during experiments changed the condition of equal volume fractions of D_2O and octane to some extent, the phase diagram is not expected to change appreciably from that of the oil-water isometry.

For $\gamma=15.77$ and $T=18.50\,°\text{C}$, corresponding to case (a) in Table II, Fig. 2(b) shows a bulk SLD of 2.96×10^{-6} $(1/\text{Å}^2)$, different from the theoretical value 2.51×10^{-6} $(1/\text{Å}^2)$ due to octane evaporation. This means that the surfactant concentration γ is actually higher than 15.77%. In fact, it was estimated to be $\gamma'=17.40\%$ (see Table I). In Fig. 2(b), the SLD profile displays a layered structure. On the air-microemulsion interface, there is an 85-Å surface layer of average density 5.0×10^{-6} $(1/\text{Å}^2)$. The front surface of this layer reaches 6.0×10^{-6} $(1/\text{Å}^2)$ which is closest to the value of pure D_2O $[6.398\times10^{-6}$ $(1/\text{Å}^2)]$. As discussed in Sec. III, the finite-Q range of the experimental data has the effect of artificially decreasing the height of the surface layer in the inversion, so the difference between the height of this high-density layer

TABLE II. Layering parameters of microemulsions. Columns marked Fig. 8(a), Fig. 8(b), and Fig. 8(c) correspond to the three solid dots (Fig. 1) marked (a), (b), and (c), respectively. The column marked "SANS" is for the neutron-scattering measurement on a bulk microemulsion.

Cases Parameters	Fig. 8(a)	Fig. 8(b)	Fig. 8(c)	SANS (bulk)
T (°C)	18.50	21.00	23.20	23.40
γ' (%)	17.40	17.07	11.46	12.00
ξ (Å)	96	140	132	148
D (Å)	196	187	348	342
D/ξ	2.04	1.33	2.64	2.31

and that of pure D_2O is due to the finite resolving power of the data range. This means it is possible that this layer is actually a pure D_2O layer, although the actual D_2O density 6.398×10^{-6} ($1/\text{Å}^2$) manifests itself at a decreased value of 5.0×10^{-6} ($1/\text{Å}^2$). The remaining ambiguity can be partly removed by referring to the density of the surface layer in Fig. 3(b) where the full height of pure D_2O was recovered during inversion. So one may conclude that there is an 85-Å-thick D_2O-rich, if not pure-D_2O, layer on the microemulsion surface. The computed Debye correlation function from the SLD profile in Fig. 2(b) is given in Fig. 8(a). This function can be fitted into Eq. (12) with two parameters $\xi=96$ Å and $D=196$ Å, which means $D/\xi=2.07$ (see Table II). The fact that the correlation length of oscillations is $\xi=96$ Å which is less than the repeat distance $D=196$ Å suggests that only the nearest neighbors are significantly correlated. This means that there is no surface-induced long-range order in the microemulsion for $\gamma=17.40\%$ and $T=18.50\,^{\circ}\text{C}$. From Fig. 2(b), we see that the layered structure of the SLD density extends into the bulk by about 500 Å.

For the microemulsion at $\gamma=15.77$ and $T=21.00\,^{\circ}\text{C}$ shown in Fig. 3(b), corresponding to case (b) in Table II, it has a bulk density of 2.87×10^{-6} ($1/\text{Å}^2$). Compared to Fig. 2(b), this sample has suffered less octane evaporation because the density is closer to the initial theoretical value of 2.51×10^{-6} ($1/\text{Å}^2$). The effective surfactant concentration is estimated to be $\gamma'=17.07\%$. The SLD profile in Fig. 3(b) exhibits a more pronounced layered structure than that in Fig. 2(b). We find that the first layer is pure D_2O with a density of 6.398×10^{-6} ($1/\text{Å}$) and the thickness is about 67 Å, smaller than the thickness (85 Å) of the first layer in Fig. 2(b). To analyze the layering structure quantitatively, the Debye correlation function is calculated from Fig. 3(b) and plotted in circles in Fig. 8(b). It is then fitted (see Table II) into Eq. (12) with $\xi=140$ Å, $D=187$ Å, and $D/\xi=1.33$ [plotted as a solid line in Fig. 8(b)]. Compared with the previous experiment, the water-water domain repeat distance $D=187$ Å from Fig. 8(b) has come very close to the value $D=196$ Å of the previous case, as the sample compositions in both cases are very close. However, the coherent length $\xi=140$ Å is appreciably larger than the previous value $\xi=96$ Å. The reason is that $T=21.00\,^{\circ}\text{C}$ has the sample closer to the lamellar phase boundary (Fig. 1) and consequently, the ordering is more pronounced. For same reason, there is a larger penetration depth (about 1000 Å).

Figure 4(b) shows the reconstructed profile for the microemulsion at $\gamma=10.55\%$ and $T=23.20\,^{\circ}\text{C}$, corresponding to case (c) in Table II. The effective bulk SLD is 3.05×10^{-6} ($1/\text{Å}^2$) as compared to the theoretical value of 2.65×10^{-6} ($1/\text{Å}^2$). From this, the effective surfactant concentration is estimated to be $\gamma'=11.46\%$ (see Table I). The reconstructed profile in Fig. 4(b) exhibits surface layering with two types of layer thicknesses. One is the surface layer of 250 Å and the other is the uniform 125-Å thickness of the following layers. The 250-Å layer is the result of the wide bump around $Q=0.02$ Å^{-1} in Fig. 4(a). Because the set of data for this inversion has the shortest range of Q (0.038 Å^{-1}), the surface D_2O layer SLD height is not fully recovered. The layering structure propagates into the bulk with a long penetration depth, of about 2000 Å. The computed Debye correlation functions can be fitted into Eq. (12) with two parameters $\xi=132$ Å and $D=348$ Å (Table II). A previous SANS experiment on this kind of microemulsion at $\gamma=12\%$ ($\phi_s=0.144$) and $T=23.40\,^{\circ}\text{C}$, very close to the phase point where the reflectivity measurement of case (c) in Table II was made, gave $\xi=148$ Å and $D=342$ Å. These ξ and D values agree reasonably well with those obtained by fitting the computed Debye correlation function into Eq. (12).

In summary, we make the following conclusions: (a) There exists a D_2O layer on the surface of the microemulsions; (b) the presence of the air-microemulsion surface induces alternate layering of water and oil, which penetrates deep into the bulk; (c) the period of the layering is well correlated with the domain-domain repeat distance of the bulk microemulsions and is a function of γ; (d) the penetration depth of the layered structure ranges from 500 to 2000 Å, depending on the position of the microemulsion in the phase diagram in such a way that it is longer when the phase point is closer to the three-phase body. Besides, it should be noted that conclusion (a) is not intended to rule out the existence of a monolayer of $C_{10}E_4$ on the surface of water. However, the confirmation of such a surfactant layer is beyond the resolution of the measurements we have made. To substantiate this point, a layer with an SLD of 0.522×10^{-6} ($1/\text{Å}^2$) and thickness $=10$ Å ($\sim$ length of the hydrophobic tail of $C_{10}E_4$) was added to each of the profiles in Figs. 2(b), 3(b), and 4(b), and the corresponding reflectivities were calculated. By comparing these reflectivities to those in the absence of the 10-Å layer, we found that the difference due to the presence of the 10-Å layer was about 4% on the average, which was in fact comparable to the experimental errors. Another observation is that such a difference occurred mostly at the high end of the Q axis and the critical region is least affected. This means that more experimental data points of sufficient precision are needed at larger Q values (i.e., a larger Q range) in order to resolve the existence of the surfactant monolayer on the surface of water.

ACKNOWLEDGMENTS

Xiao-Lin Zhou is grateful for financial support from Argonne National Laboratory. Research work of Sow-Hsin Chen is supported by a grant from the Materials Science Division of the DOE.

---

[1] M. Kahlweit, R. Strey, and G. Busse, J. Phys. Chem. **94**, 3881 (1990).

[2] F. Lichterfeld, T. Schmeling, and R. Strey, J. Phys. Chem. **90**, 5762 (1986).

[3] S. H. Chen, S. L. Chang, R. Strey, J. Samseth, and K. Mortensen, J. Phys. Chem. **95**, 7427 (1991); S. H. Chen, S. L. Chang and R. Strey, J. Chem. Phys. **93**, 1907 (1990).

[4] M. Teubner and R. Strey, J. Chem. Phys. **87**, 3195 (1987); W. Jahn and R. Strey, J. Phys. Chem. **92**, 2294 (1988).

[5] S. H. Chen, S. L. Chang, and R. Strey, Prog. Colloid Polym. Sci. **81**, 30 (1990).

[6] S. H. Chen and S. L. Chang, J. Appl. Cryst. **24**, 721 (1991).

[7] D. K. Schwartz, A. Braslau, B. Ocko, and P. S. Pershan, Phys. Rev. A **38**, 5817 (1988).

[8] M. Kotlarchyk, S. H. Chen, J. S. Huang, and M. W. Kim, Phys. Rev. Lett. **53**, 941 (1984).

[9] K. A. Dawson, Phys. Rev. A **35**, 1766 (1987).

[10] B. M. Ocko, A. Braslau, P. S. Pershan, J. Als-Nielsen, and M. Deutsch, Phys. Rev. Lett. **57**, 94 (1986).

[11] P. S. Pershan, A. Braslau, A. H. Weiss, and J. Als-Nielsen, Phys. Rev. A **35**, 4800 (1987).

[12] G. Swislow, D. Schwartz, B. M. Ocko, P. S. Pershan, and J. D. Litster, Phys. Rev. A **43**, 6815 (1991).

[13] K.-V. Schubert, R. Strey, and A. Kahlweit, J. Coll. Interf. Sci. **141**, 21 (1991).

[14] Xiao-Lin Zhou, S.-H. Chen, and G. P. Felcher, J. Phys. Chem. **95**, 9025 (1991).

[15] Xiao-Lin Zhou, S.-H. Chen, and G. P. Felcher, Phys. Rev. A **46**, 1839 (1992).

[16] G. Parratt, Phys. Rev. **95**, 359 (1954).

[17] Xiao-Lin Zhou and Sow-Hsin Chen (unpublished).